Rare Met.
https://doi.org/10.1007/s12598-025-03454-0

RARE METALS

ORIGINAL ARTICLE

High-permittivity and low-hysteresis dielectric elastomer for near-free dynamic hysteresis and high-fidelity strain sensors

Yu-Shu Wang, Run-Hui Zhou, Jiao-Ya Huang, Bo-Ning Sun, Ze-Min Li, Zi-Yu Chen, Zhuo-Yu Song, Wen-Chao Gao, Cao-Feng Pan*

Received: 9 March 2025 / Revised: 19 May 2025 / Accepted: 19 May 2025

Abstract Stretchable strain sensors are a crucial component in various applications, such as wearable devices, human–machine interfaces, and soft robotics. Hence, strain sensors with low hysteresis, high fidelity, and accurate sensing ability are urgently required for the precise measurement of large and high-frequency dynamic deformations. However, the existing hysteresis of the current functional materials utilized in strain sensors significantly impedes the achievement of these properties. Herein, we introduce an ultralow dynamic hysteresis capacitive strain sensor using a low-hysteresis and high-relative-permittivity ionic liquid-elastomer composite as the dielectric material. Based on the low-hysteresis dielectric, the prepared capacitive strain sensors exhibit ultralow electrical hysteresis (2.20% at a strain rate of 100% s^{-1} and strain of 100%) and maintain low electrical hysteresis (4.35%) even under extremely high strain rates and large dynamic strain loads (a strain rate of 500% s^{-1} and strain of 100%). Moreover, the strain sensor manifests exceptional cyclic stability under 50,000 cycles of 100% strain at a strain rate of 200% s^{-1}; the response curves remain nearly identical throughout these 50,000 cycles. Furthermore, the ultralow-hysteresis strain sensor was successfully applied to accurate and reliable real-time human–machine interactions, revealing its great potential in various fields, including electronic skin, flexible robotics, wearable electronics, and virtual reality.

Keywords Flexible electronics; Strain sensors; Low hysteresis; Dielectric elastomer; Human–machine interaction

Yu-Shu Wang, Run-Hui Zhou and Jiao-Ya Huang have contributed equally to this work.

Supplementary Information The online version contains supplementary material available at https://doi.org/10.1007/s12598-025-03454-0.

Y.-S. Wang, C.-F. Pan*
Center on Nano-Energy Research, Guangxi Key Laboratory for the Relativistic Astrophysics, School of Physical Science & Technology, Guangxi University, Nanning 530004, China
e-mail: pancaofeng@buaa.edu.cn

Y.-S. Wang, R.-H. Zhou, Z.-Y. Chen, C.-F. Pan
Institute of Atomic Manufacturing, Beihang University, Beijing 100191, China

J.-Y. Huang, B.-N. Sun, Z.-M. Li, W.-C. Gao, C.-F. Pan
CAS Center for Excellence in Nanoscience, Beijing Key Laboratory of Micro-Nano Energy and Sensor, Beijing Institute of Nanoenergy and Nanosystems, Chinese Academy of Sciences, Beijing 101400, China

Z.-Y. Song
Department of Engineering Mechanics, Dalian University of Technology, Dalian 116024, China

1 Introduction

With the rapid development of artificial intelligence and the Internet of Things, strain sensors have become indispensable in a wide range of applications [1–5], including soft robotics [6–12], motion detection [13–19], virtual reality [20–22], human–machine interfaces [23–26], and remote industrial systems [27–29]. The precise and accurate measurement of high-frequency dynamic deformations is essential for practical applications because the speed of human limb movements in real life generally exceeds 100 mm min^{-1}, with strain rates higher than 20% s^{-1} [30]. The signal fidelity refers to the similarity between a signal and its original version during transmission or processing.

Published online: 21 July 2025

A higher fidelity corresponds to superior signal reconstruction and reduced distortion. Hysteresis is a critical metric of signal fidelity and refers to the distinct response curves observed between the loading and unloading processes. The lower the hysteresis is, the smaller the difference between the loading and unloading curves is. Consequently, strain sensors that possess low hysteresis, high fidelity and precision, robust stability, and good reliability are highly desired to ensure the accurate capture of precise dynamic strain signals [1, 31–34].

Recent research has largely focused on resistive and capacitive strain sensors [35, 36], which are relatively simple to fabricate and characterize. Capacitive sensors exhibit superior performance metrics in terms of high linearity and long-term stability compared to their resistive counterparts [28, 37–41]. This advantage stems from the fundamental operational principle of capacitive strain sensors, which employ geometry-dependent deformation mechanisms (i.e., changes in the overlap area between electrodes) to achieve precise mechanical strain quantification [42–44]. Nevertheless, conventional dielectric elastomers utilized in capacitive strain sensors are constrained by their intrinsic viscoelastic properties, manifesting significant hysteresis during deformation recovery, which adversely affects the measurement fidelity. Concurrently, achieving high-permittivity elastomers for signal-to-noise ratio enhancement in such sensors [23] requires the incorporation of inorganic fillers to improve the dielectric properties. Paradoxically, this approach improves the electrical performance while aggravating hysteresis [45]. For example, incorporating ferroelectric materials into silicone rubber can increase the dielectric constant by a factor of three, but this results in serious degradation of the mechanical properties [46]. Structural design offers an alternative approach for mitigating some of the limitations imposed by material properties. Wavy, wrinkled, helical, and origami-inspired designs have been explored, and relatively high sensitivity, large stretchability, and reduced hysteresis have been achieved using different structures [47–51]. However, the current study mainly investigated sensing performance under quasi-static or low-speed tensile conditions (typically < 10 mm s^{-1}, strain rates $< 42\%$ s^{-1}, Table S1) [28, 52–58], indicating that the viscoelasticity of materials still has limitations on the sensing performance. Precise and accurate detection of large high-frequency strain signals remains challenging.

Herein, we propose an ultralow dynamic hysteresis capacitive strain sensor. This strain sensor employs an ionic liquid-elastomer composite dielectric with low-hysteresis and high-relative permittivity. By introducing an ionic liquid (IL) into polydimethylsiloxane (PDMS), the prepared IL-PDMS composite exhibits high relative permittivity without compromising elasticity. The relative permittivity substantially improves when the IL content increases from 0 to 30 wt%. Meanwhile, the degree of hysteresis of the composites remains nearly constant with the use of different IL concentrations. As reported in our previous study, we fabricated a capacitive strain sensor using an IL-PDMS composite as the dielectric and SH-PAAm hydrogels as electrodes [59]. Based on the excellent mechanical and electrical properties of the IL-PDMS composite, the prepared strain sensor demonstrates ultralow hysteresis (2.20%) and high accuracy under dynamic conditions (100% s^{-1} strain rate with 100% strain). Remarkably, even under more extreme loading (500% s^{-1} rain rate with 100% strain), the sensors maintain a minimal hysteresis level of 4.35%. In addition to superior hysteresis performance, the sensors have outstanding cyclic stability and robustness, enduring 50,000 cycles at 100% strain and a strain rate of 200% s^{-1} without performance degradation. The response curves remained virtually identical throughout the test cycles. This result further confirmed the durability and reliability of the sensors. Based on the ultralow dynamic hysteresis and robust performance, our strain sensor was successfully applied to accurate and reliable real-time human–machine interaction. The results illustrate its enormous potential for application in electronic skins, flexible robotics, wearable electronics, and virtual reality.

2 Experimental

2.1 The preparation of composite elastomers

The PDMS prepolymer was prepared by mixing the base hydroxy-terminated polydimethylsiloxane and crosslinker (trimethoxy (1H,1H,2H,2H-heptadecafluorodecyl) silane) at a weight ratio of 8.5:1. Then, the prepolymer and ionic liquid (1-ethyl-3-methylimidazolium bis (trifluoromethylsulfonyl) imide (97%, Aladdin)) were thoroughly mixed via a shearing emulsifying mixer at a predesigned ratio (ionic liquid 0–30 wt%) to form a viscous opaque emulsion. Subsequently, dibutyltin dilaurate (95%, Sigma-Aldrich) was added at a mass ratio of 2345:1 (hydroxyl-terminated polydimethylsiloxane to dibutyltin dilaurate). For example, when 1 g of hydroxyl-terminated polydimethylsiloxane was used, 40 μL of a 10% dibutyltin dilaurate solution dispersed in methyl isobutyl ketone ($\geq$ 99.5%, Aladdin) was incorporated. After eliminating the bubbles with a stirring and defoaming machine, the emulsion was slowly transferred onto a glass sheet (50 mm × 50 mm) for spin coating (400 rad s^{-1}, 30 s). Then, a complete 4-h curing process (at 60 °C) was performed to obtain composite elastomers with distinct components.

2.2 The fabrication of SH-PAAm hydrogel pro-gel solution

The preparation was performed according to previous work [59]. Sodium hyaluronate polyacrylamide (SH, Shanxi Carryherb Bio Co., Ltd.) was dissolved in deionized water to form an SH aqueous solution (2.5 wt%). Then, acrylamide (AAm, 99%, Aladdin) was dissolved in the SH aqueous solution (at a ratio of 1:3) and stirred manually at room temperature until fully dissolved. A LiCl powder (16.5 wt%), glycerin (13.8 wt%), N, N-methylenebisacrylamide cross-linking agent (MBAA, 99%, Aladdin) (0.4 wt% of AAm), polyethylene glycol diacrylate (PEGDA, Aladdin) (0.42 wt% of AAm), and Irgacure 2959 photoinitiator (0.2 wt%) were added in sequence and manually stirred at room temperature. The mixed solution was then incubated for 24 h at room temperature to remove the air bubbles. VHB (400 μm, VHB4920, 3 M) was the dielectric for the high-hysteresis capacitive strain sensor in this work. Polydimethylsiloxane (PDMS, BD film KRR100, Hangzhou Guinie Advanced Materials Co., Ltd.) was used as the encapsulation material. Benzophenone (Sigma-Aldrich, B9300) was dispersed in ethanol as a surface treatment reagent.

2.3 The fabrication of the low-hysteresis strain sensor

The surface of a 50 mm (length) × 15 mm (width) sample of PDMS/$IL_{0.3}$ was treated with benzophenone solution (10 wt%). A gold electrode deposited on PET (approximately 5 mm in width) was attached to the side of the PDMS/$IL_{0.3}$, and a rectangular hollow shape (the size of the hollow part was 30 mm (length) × 5 mm (width)) was placed on the surface of the PDMS/$IL_{0.3}$. Subsequently, the SH-PAAm hydrogel pro-gel solution was poured into the mold of the PET film and photocured under ultraviolet light for 10 min. Subsequently, a thin layer of pure PDMS was spin-coated on its surface, and then, KRR100 PDMS (50 mm (length) × 15 mm (width)) was attached to the layer. After fully curing and repeating the above steps, the thin gold electrode, SH-PAAm hydrogel, and encapsulation layers were sequentially assembled at the other side of the PDMS/$IL_{0.3}$. The prepared sensors had an overlapping area of 10 mm × 5 mm between the upper and lower electrode plates.

2.4 The fabrication of the high-hysteresis strain sensor

A gold electrode deposited on PET (about 5 mm in width) was attached to the side of the VHB (400 μm, VHB4920, 3 M) (50 mm (length) × 15 mm (width)), and then, PET film with a rectangular hollow shape (the size of the hollow part is 30 mm (length) × 5 mm (width)) was placed on the surface of the VHB. Subsequently, the SH-PAAm hydrogel pro-gel solution was poured into the PET film mold and photocured under ultraviolet light for 10 min. Subsequently, the SH-PAAm hydrogel and VHB were encapsulated in KRR100 PDMS (50 mm (length) × 15 mm (width)) using commercial glue and set aside for approximately 24 h until the glue was fully cured. After full curing, a thin gold electrode, the SH-PAAm hydrogel, and encapsulation layers were sequentially assembled on the other side of the VHB. The prepared sensors had an overlapping area of 10 mm (length) × 5 mm (width) between the upper and lower electrode plates.

3 Results and discussion

3.1 Principle and material of the low-hysteresis strain sensor

Low-hysteresis dielectric materials are crucial for achieving low dynamic hysteresis strain sensors, whereas capacitive sensing applications simultaneously demand high relative permittivity. To reconcile these competing requirements, we introduced an IL into the superelastic PDMS polymer to create a composite that combined enhanced permittivity with retained elasticity (Fig. 1A).

The developed sensor architecture integrates hysteresis-suppressing components such as low-hysteresis and high-permittivity dielectrics, low-hysteresis hydrogel electrodes, and low-hysteresis PDMS encapsulation, achieving ultra-low-hysteresis and high-fidelity detection. In contrast, the pronounced hysteresis that exists in conventional strain sensors typically results in significant signal distortion (Fig. 1B). This distinction is mainly due to the different elasticities of the dielectric materials. PDMS is a typical superelastic material; the stress on this elastomer depends solely on the current deformation and remains unaffected by any previous deformations, thereby establishing a one-to-one correspondence between the stress and strain. Consequently, PDMS can be promptly restored to its original state after tensile release. Viscoelastic materials, such as VHB, consume part of their energy owing to their viscosity, which makes them unable to recover immediately after tensile release (Fig. 1C).

3.2 Characterization of the dielectric layer materials

VHB is widely used as a dielectric material in flexible strain sensors. To characterize the dielectric performance, we systematically measured the relative permittivity of

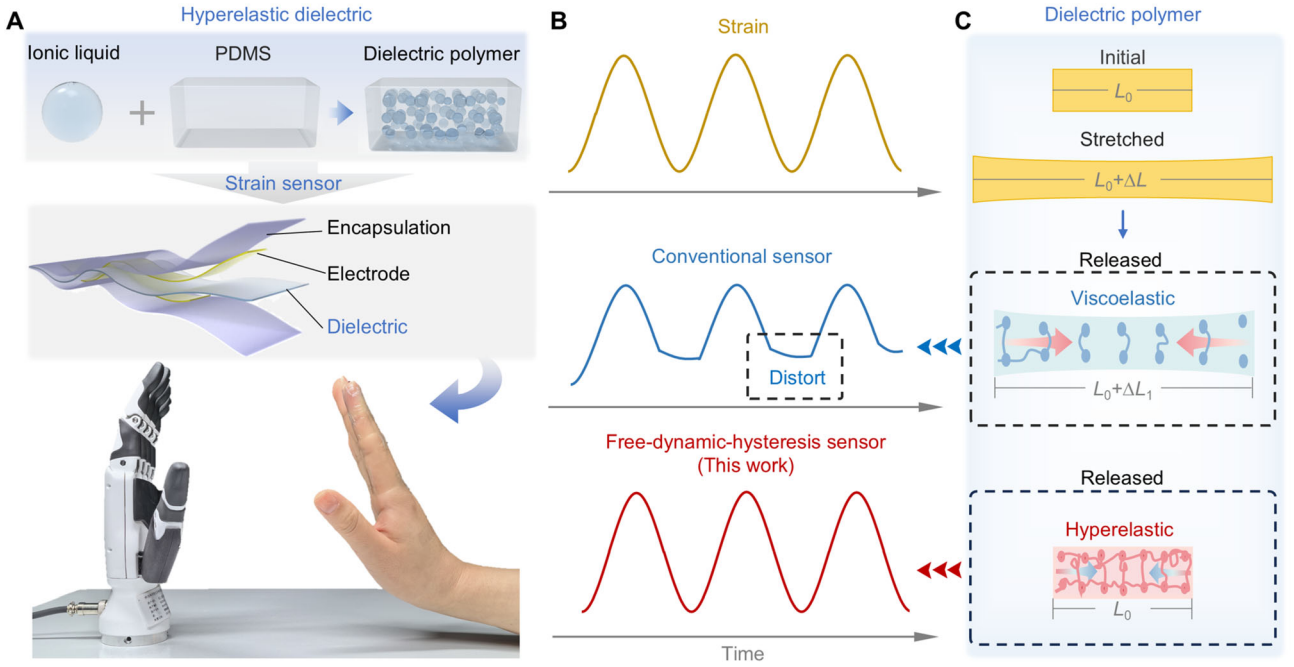

Fig. 1 Principle and material of the low-hysteresis strain sensor. **A** The sensor in this work is composed of a superelastic dielectric material, a superelastic encapsulation layer, and a low-hysteresis hydrogel; **B** the free-dynamic-hysteresis strain sensor provides a high-fidelity signal, while the traditional strain sensor provides a low-fidelity signal under the same strain; **C** the superelastic dielectric material immediately returns to its original state after stretching, while the viscoelastic dielectric material requires a certain period to recover

conventional VHB, pristine PDMS, and IL-modified PDMS composites (0–30 wt% IL). As shown in Fig. 2A, the relative permittivity of the dielectric elastomer gradually increased with increasing IL content and reached 10.88 at 10 kHz for PDMS mixed with 30 wt% IL (PDMS/$IL_{0.3}$). This relative permittivity was a 4.6-fold improvement over that of pristine PDMS (2.36) and a 3.2-fold improvement over that of VHB (3.35). This controlled permittivity escalation demonstrates the effectiveness of our strategy of introducing an IL to improve the relative permittivity of PDMS.

Current research lacks a systematic standard for characterizing hysteresis [60–62]. For elastomer materials, strain is a time-dependent variable; therefore, ensuring consistent time intervals when measuring stress–strain cycles at the same level of strain is imperative. To further standardize the measurement parameters, we introduce the concept of strain rate $\varepsilon(t)$:

$$\varepsilon(t) = \frac{d\varepsilon}{dt} = \frac{dL(t)}{L_0} \times \frac{1}{dt} \quad (1)$$

where ε is the strain rate, $L(t)$ is the length of the sample at time t, and L_0 is the original length. Under usual circumstances, the minimum strain rate of the human joint during daily movement is approximately 20% s^{-1} [35], and the maximum strain is 80%. Consequently, the stress–strain curves of all-dielectric elastomers in this study were measured at a 20% s^{-1} strain rate and 100% strain (Fig. 2B).

The degree of hysteresis (DH) is typically used to evaluate the degree of hysteresis of strain sensors and can be divided into the degree of mechanical hysteresis (DMH) and the degree of electrical hysteresis (DEH) according to different measurements. In this study, the DMH was defined as follows:

$$\mathrm{DMH} = \frac{|A_{ms} - A_{mr}|}{A_{ms}} \times 100\% \quad (2)$$

where A_{mr} is the area between stress and strain when stretched from 100% to 0 strain, and A_{ms} is the area between stress and strain when stretched from 0 to 100% strain. The integral functions of stress with respect to strain for A_{ms} and A_{mr} were determined by integrating the stress–strain curves over the 0–100% (loading phase) and 100%–0 (unloading phase) strain ranges, respectively. $|A_{mr}-A_{ms}|$ is the area difference between the response and strain curves of the stretched and released states. The DMH calculation method is shown in Fig. S1.

Based on the stress–strain curve in Fig. 2B, we calculated and analyzed the DMH of the dielectric elastomer. Quantification of the DMH revealed approximately 8% values for both pristine PDMS and IL-modified composites (Fig. 2C). This demonstrated that the hyperelastic behavior

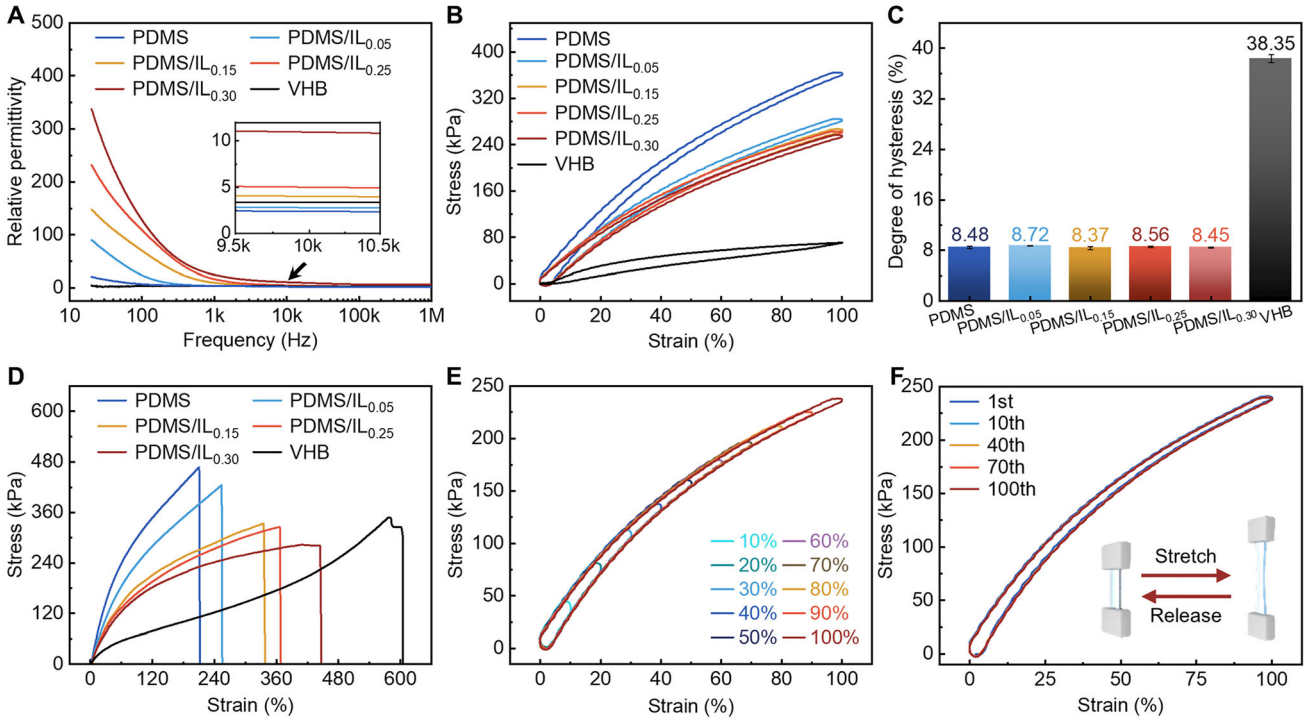

Fig. 2 Characterization of dielectric layer materials: **A** relative permittivity of PDMS with different mass fractions of ionic liquid (IL) and relative permittivity of VHB; **B** stress–strain curves of PDMS with different mass fractions of IL and VHB; **C** DMH of PDMS with different mass fractions of IL and DMH of VHB; **D** fracture elongation curves of PDMS with different mass fractions of IL and VHB; **E** stress–strain curves of PDMS/$IL_{0.3}$ under various strains; **F** cyclic stability of PDMS/$IL_{0.3}$ over 100 cycles, where (**B**, **E**, and **F**) measurements are all carried out at a 20% s^{-1} strain rate

of PDMS was not disrupted by the integration of ionic liquid. Notably, these materials maintained superior hysteresis characteristics over conventional VHB (38.35% DMH). In addition, with an increase in the IL content, the Young's modulus gradually decreased, and the fracture strain gradually increased (Fig. 2D). Although the strain of PDMS/$IL_{0.3}$ at fracture is still lower than that of VHB, the strain is far beyond the maximum strain that human joints can achieve. PDMS/$IL_{0.3}$ demonstrates exceptional multifunctional performance through optimized permittivity, low mechanical hysteresis, and a low Young's modulus of the elastomer. However, practical dielectric layer applications require further validation of stable mechanical hysteresis under various strains and cycle numbers. Therefore, we conducted measurements on its stress–strain curve at different strain levels (at a constant strain rate of 20% s^{-1}) (Fig. 2E) and 100 stress–strain cycles (Fig. 2F). This material exhibits nearly identical mechanical hysteresis under both high and low strains, and no significant alteration in the mechanical hysteresis was observed after multiple cycles. PDMS/$IL_{0.3}$ has been demonstrated to be an exemplary dielectric layer material with minimal hysteresis (8.45% at a 20% s^{-1} strain rate and 100% strain), high relative permittivity (10.88), high stretchability (100%), and cyclic stability. Figure S2 compares the experimental stress relaxation data of PDMS/$IL_{0.3}$ and VHB with theoretical calculation results, enabling determination of the viscoelastic parameters G_i and τ_i in the stress component σ_V. The fitted parameters are listed in Table S2. Figure S3A, B presents the experimental versus theoretical stress–strain curves for both materials, with goodness-of-fit values of 0.9915 (PDMS/$IL_{0.3}$) and 0.9988 (VHB). Both goodness-of-fit values exceeded 0.99. This validates the strong consistency between our theoretical framework and the experimental observations. Corresponding material parameters μ_p and α_p are listed in Table S3.

3.3 Design and characterization of strain sensors

Our former work showed that the SH-PAAM hydrogel is a water-retaining hydrogel material with a low DMH [59]. The SH-PAAM hydrogel demonstrated a remarkably low DMH of 4.40% under dynamic loading at a 20% s^{-1} strain rate with 100% applied strain (Fig. S4). Based on this, we constructed a strain sensor by sandwiching a layer of PDMS/$IL_{0.3}$ between two layers of SH-PAAM hydrogel (Fig. 3A), and the DMH of the sensor was merely 4.98% (Fig. S4). Hereafter, we refer to the strain sensor as a PDMS/$IL_{0.3}$-sensor for concision, unless otherwise

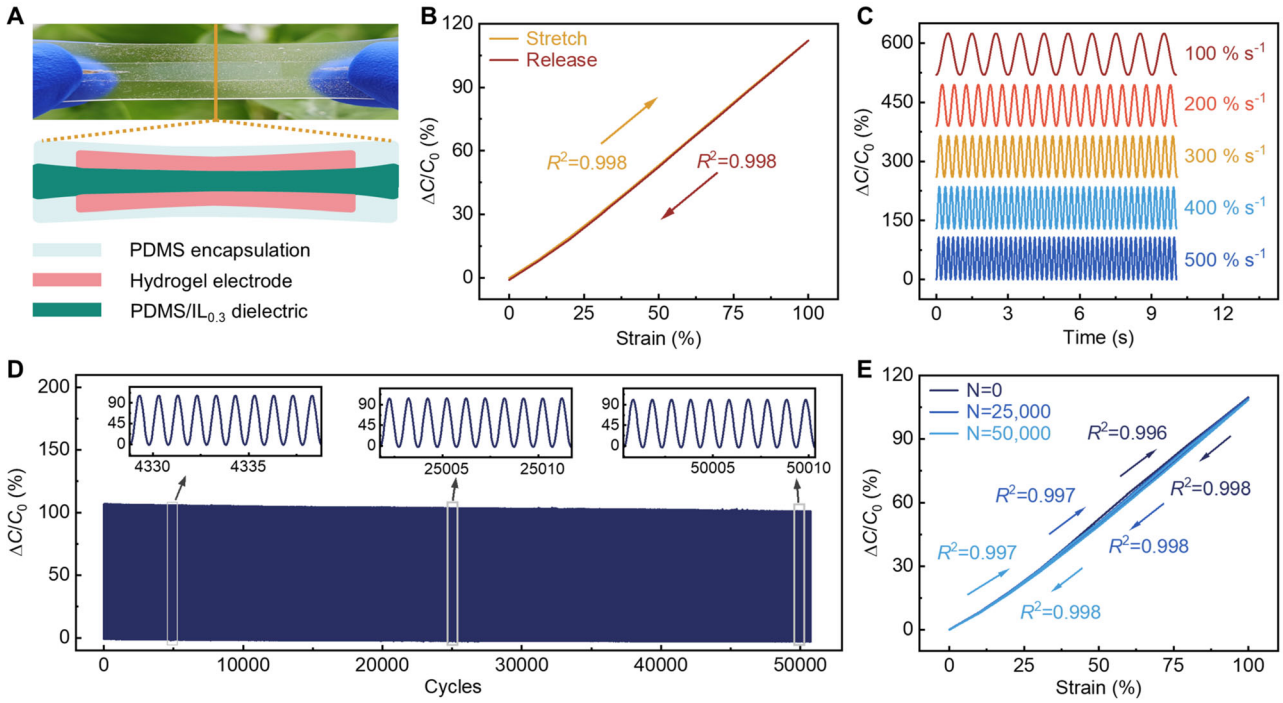

Fig. 3 Performance characterization of the flexible strain sensor: **A** schematic diagram of the device structure of low-hysteresis sensor during tension; **B** the linearity of the stretch and release process; **C** the capacitance changes of the sensor under sinusoidal motion at different frequencies under 100% strain; **D** stability of the relative capacitance changes of the PDMS/$IL_{0.3}$-sensor over 50,000 stretching cycles at a strain of 100%; **E** the linearity before cycles, at approximately 25,000 cycles, and after cycles

specified. As shown in Fig. S5, we conducted in situ stretching of the PDMS/$IL_{0.3}$-sensor. During the stretching of the strain sensor from 0% to 200%, no relative slippage is found between the layers of the strain sensor. Additionally, the interlayer bonding strength of the capacitive strain sensor of more than 99.23 N m^{-1} (Fig. S6) indicates strong interlayer interactions.

Based on the capacitive response of steady-state step test shown in Fig. S7, the sensitivity under varying strains and the linearity ($R^2 > 0.998$) (Fig. 3B) can be derived. As illustrated in Fig. S8, sensitivity progressively increases with strain and rises from 0.89 at 10% strain to 1.12 at 100% strain. This enhancement stems from ionic liquid incorporation, which alters the polarization orientation within the dielectric elastomer during stretching, thereby modifying the relative dielectric constant [63].

The sensing performance of the PDMS/$IL_{0.3}$-sensor was systematically characterized with varying strain rates (100–500% s^{-1}). As shown in Fig. 3C, the PDMS/$IL_{0.3}$-sensor consistently exhibits outstanding sensing capabilities under 100% strain at different strain rates. Extended durability testing simulating human joint kinematics (100% strain and a 200% s^{-1} strain rate) [64] confirmed stable operation over 50,000 cycles (Figs. 3D and S9). To further elucidate the performance evolution before and after cyclic loading, we statistically analyzed the performance metrics at different stages of the cycling process. These metrics include sensitivity, hysteresis, and capacitance variation. As shown in Table S4, these slight changes in performance indicate that the PDMS/$IL_{0.3}$-sensor maintains exceptional performance even after 50,000 cycles. From the 50,000-cycle capacitance variation profiles, 100 curves were uniformly sampled for the statistical analysis of maximum values, minimum values, and amplitudes. Calculated mean values with standard deviations are as follows: maximum 103.57 (σ = 1.51), minimum –2.31 (σ = 0.53), and amplitude 105.88 (σ = 1.00) (Fig. S10). These metrics confirm the sustained high reliability over 50,000 cycles. Linearity measurements recorded before testing, after approximately 25,000 cycles, and post-50,000 cycles (Fig. 3E) demonstrate exceptional linearity retention throughout full cycling. This facilitates mass production without the need for calibration before use. These results indicate that the PDMS/$IL_{0.3}$-sensor with a multilayer composite structure has good comprehensive performance in real-time signal sensing.

3.4 Electrical hysteresis of the strain sensor

As described earlier, the hysteresis comprises two components: DMH and DEH. The PDMS/$IL_{0.3}$-sensor exhibits a relatively low DMH (4.98%; Fig. S4). The DEH of the

sensor was further characterized to elucidate its properties. VHB is extensively used in the fabrication of capacitive strain sensors because of its superior stretchability and inherent self-adhesion [40–42, 54]. However, the inherent viscoelasticity of the VHB can result in significant hysteresis. Here, a strain sensor with VHB as the dielectric layer was used as the control (named VHB-sensor). The two sensors are distinguished only by the dielectric layer. The two sensors were fixed to a linear motor (Fig. S11), and the motion of the sensor was controlled. When the two sensors were released after stretching, the PDMS/$IL_{0.3}$-sensor immediately recovered its initial state, whereas the VHB-sensor did not promptly revert to its initial state and exhibited an arched shape (Fig. 4A).

Research on electrical hysteresis can be categorized into static and dynamic electrical hysteresis according to the applied measurements. Figure 4C, D shows the capacitance changes of the PDMS/$IL_{0.3}$-sensor and VHB-sensor, respectively, under different strains. The recovery time was used to characterize the static electrical hysteresis of the sensor. The inherent motion duration of the linear motor was included in the sensor recovery time measurements because of the infeasibility of removing this parameter during the experimental quantification. However, considering that the linear motor operated under identical program instructions (maximum speed: 500 mm s^{-1}; maximum acceleration: 100 mm s^{-2}), the recovery time for both sensors can be inferred to encompass an identical duration of linear motor motion. Hence, we can use the recovery time marked in the figure instead of the actual recovery time to characterize the static electrical hysteresis of the sensor. Multiple measurements were conducted to calculate the recovery times for various strains (Fig. 4E). At a low strain level of 10%, the recovery time of the VHB-sensor is approximately 0.66 s. In contrast, the PDMS/$IL_{0.3}$-sensor exhibits a recovery time of approximately 0.10 s. This recovery time is 0.56 s less than the VHB-sensor. At a higher level of 100%, the recovery time for the VHB-sensor reaches approximately 4.86 s. Meanwhile, for the PDMS/$IL_{0.3}$-sensor, the recovery time is only 0.22 s and decreases by approximately 4.64 s. The recovery time of the PDMS/$IL_{0.3}$-sensor is significantly lower than that of the VHB-sensor.

The influence of hysteresis becomes more pronounced at large strains and high strain rates. Therefore, we conducted further investigations into the dynamic hysteresis of the two sensors. Figure 4F, G illustrates the variations in capacitance signals of PDMS/$IL_{0.3}$-sensor and VHB-sensor, respectively, at different motion strain rates under a strain of 100%. The capacitance changes generated by the PDMS/$IL_{0.3}$-sensor are nearly identical during both stretching and release, whereas the capacitance changes of the VHB-sensor show significant disparities. These disparities are primarily evident in the following two aspects. On the one hand, the capacitance changes during the release stage of the VHB-sensor exhibit a significant deviation compared to that of the stretching stage. On the other hand, when the strain returned to 0%, an approximately 8% deviation is found compared to its initial value, suggesting that the VHB-sensor fails to fully recover its initial state after undergoing a stretch–release cycle. The dynamic hysteresis of the two sensors was investigated quantitatively. Figure 4B illustrates the principles and calculation methods employed in our study. The area enclosed by the change in capacitance and the determined time interval during stretching is defined as A_{es}, and the area enclosed by the change in capacitance and time during release is defined as A_{er}. The difference between these two areas reflects the accumulated hysteresis, which is normalized by dividing by A_{es}. This normalization enabled us to quantitatively compare the dynamic DEH across different strain sensors.

DEH was quantified across varying strain rates at 100% strain using an established analytical method (Fig. 4H). At the strain rate of 100% s^{-1}, the PDMS/$IL_{0.3}$-sensor exhibits an electrical hysteresis of merely 2.20%, whereas the VHB-sensor demonstrates a significantly higher value of 8.83%. When subjected to a 500% s^{-1} strain rate (Video S1), these values increased to 4.36% and 20.36%, respectively. This highlights that the DEH of the PDMS/$IL_{0.3}$-sensor is approximately threefold lower than that of the VHB-sensor. We gradually increased the actuation velocity of the linear motor and monitored the real-time dynamic responses of both sensors under controlled strain–rate variations. The PDMS/$IL_{0.3}$-sensor exhibited exceptionally high-fidelity detection, with capacitance changes that were highly coincident with the theoretical motion curve (Fig. 4I). Conversely, the capacitance variation of the VHB-sensor increasingly deviates from the theoretical motion curve as the motion velocity gradually increases (Fig. 4J). The PDMS/$IL_{0.3}$-sensor is superior to the VHB-sensor with regard to both static and dynamic DEH and exhibits negligible hysteresis when subjected to stretching-releasing cycles.

3.5 Application of the low-hysteresis sensor in human motion monitoring

The unprecedentedly low dynamic DEH and cyclic stability allow the accurate capture of the movements of various joints. The ability of the PDMS/$IL_{0.3}$-sensor to accurately monitor exercise was verified by attaching the PDMS/$IL_{0.3}$-sensor to human joints (inset in Fig. 5). The volunteer looked straight ahead, placed the PDMS/$IL_{0.3}$-sensor in its natural state around their neck, and secured the sensor with medical tape. When the volunteer bowed their

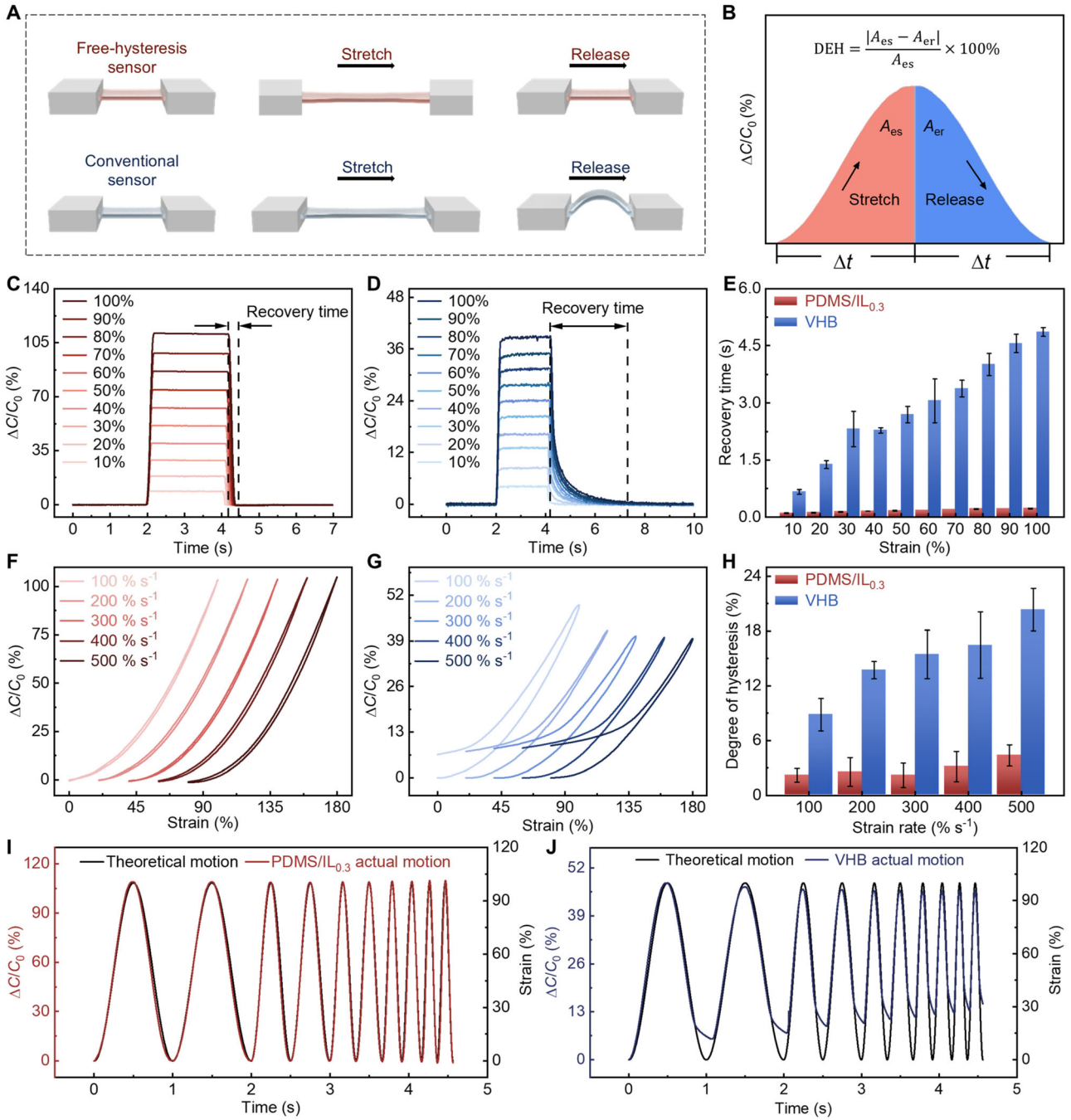

Fig. 4 Electrical hysteresis of the strain sensor: **A** schematic diagram of hysteresis of two types of sensors during stretching and releasing; **B** calculation schematic diagram of the DEH; **C** static hysteresis of the PDMS/$IL_{0.3}$-sensor; **D** static hysteresis of the VHB-sensor; **E** the recovery times of the two types of sensors; **F** dynamic hysteresis of the PDMS/$IL_{0.3}$-sensor; **G** dynamic hysteresis of the VHB-sensor; **H** DEH of the two types of sensors; **I** the PDMS/$IL_{0.3}$-sensor exhibits high-fidelity signal transmission characteristics under continuously changing motion frequency; **J** the VHB-sensor demonstrates significant signal distortion under identical operational conditions

head, the PDMS/$IL_{0.3}$-sensor was stretched. Owing to the increase in the relative area of the capacitive strain sensor and the decrease in the distance between the electrodes, the capacitance changes of the strain sensor increased. As the neck of the volunteer returned to its original state, the sensor followed the neck movement and recovered to its natural state, and the capacitance changes of the PDMS/$IL_{0.3}$-sensor gradually decreased (Fig. 5A). To monitor the movement of the elbow joint with the PDMS/$IL_{0.3}$-sensor (Fig. 5B), the PDMS/$IL_{0.3}$-sensor was placed on the elbow

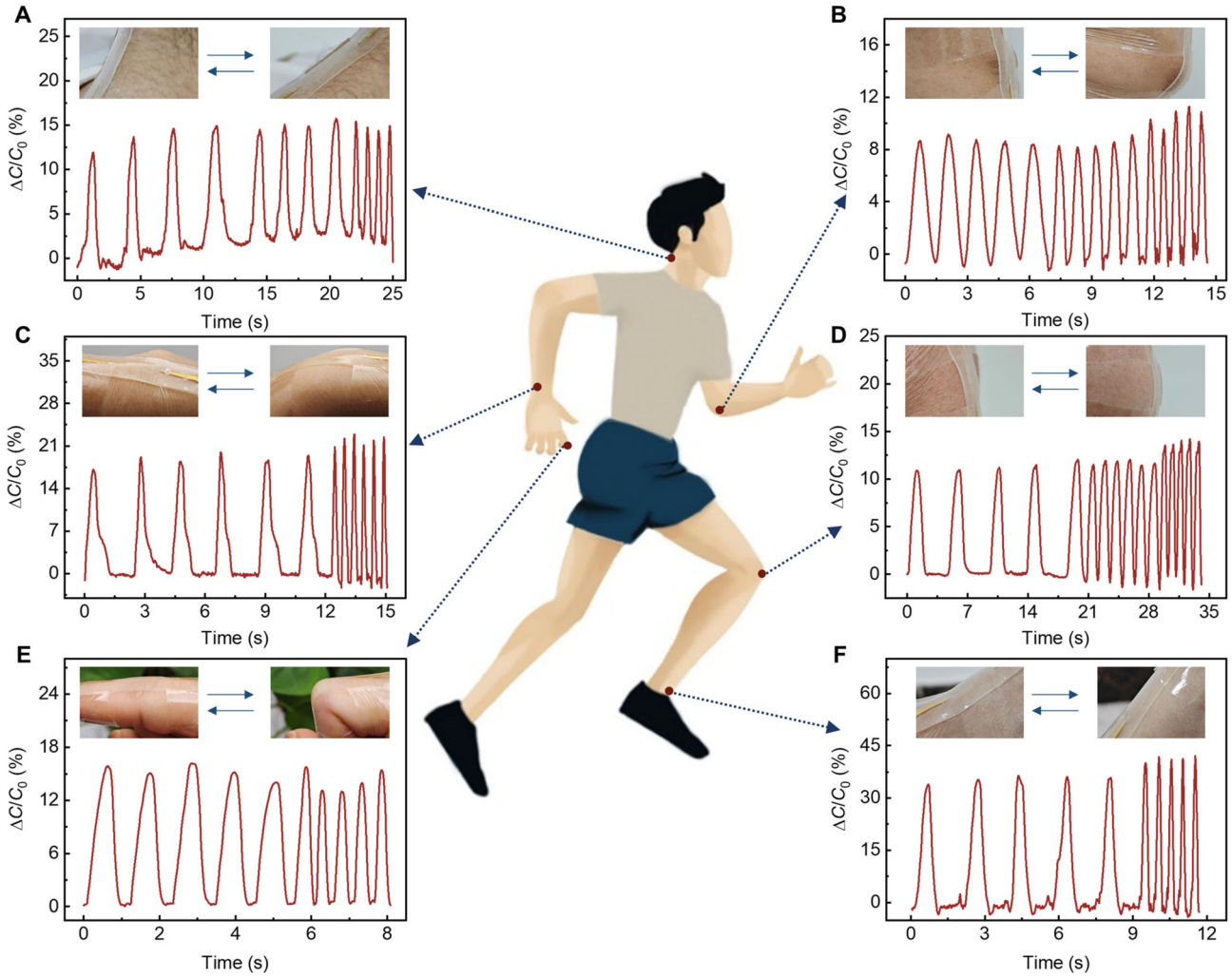

Fig. 5 Real-time capacitive signals of the low-hysteresis sensor attached to human joints: **A** neck, **B** elbow joint, **C** wrist, **D** knee joint, **E** finger, and **F** ankle joint at different motion speeds

while the forearm of the volunteer was straight, and the sensor was secured with medical tape. As the volunteer bent their forearm, the sensor gradually stretched with the bending of the elbow, and the capacitance change of the PDMS/$IL_{0.3}$-sensor gradually increased. Owing to the extremely short recovery time of the PDMS/$IL_{0.3}$-sensor, the capacitance of the sensor changed from increasing to decreasing immediately when the volunteer began to straighten the forearm. The monitoring of the PDMS/$IL_{0.3}$-sensor on the movement of the wrist joint (Fig. 5C), knee joint (Fig. 5D), finger joint (Fig. 5E), and ankle joint (Fig. 5F) indicates that the strain sensor prepared in this study exhibits real time, accurate monitoring of various joints.

In addition, to verify the precise measurement of the sensor at higher movement speeds, we increased the speed of joint movement and recorded the changes in the capacitance of the PDMS/$IL_{0.3}$-sensor. During the monitoring of movement at various joints, the wrist joint completed six flexion–extension cycles within 2.79 s (Fig. 5C), with a strain rate as high as 215% s^{-1}. This indicates that the sensor still possesses the capability for real time, accurate sensing even at extremely high motion frequencies. Therefore, the PDMS/$IL_{0.3}$-sensor has great potential for wearable applications, particularly for monitoring high-speed movements.

3.6 Accurate strain sensing for robot operation

The ability of the PDMS/$IL_{0.3}$-sensor to accurately monitor exercise was verified by attaching the PDMS/$IL_{0.3}$-sensor to smart robotic hands (inset in Fig. 6). Video S2 shows the hysteresis of the electrical signals from the two sensors after continuous motion.

The PDMS/$IL_{0.3}$-sensor and VHB-sensor tracked the smart robotic hand as it underwent a sequence of

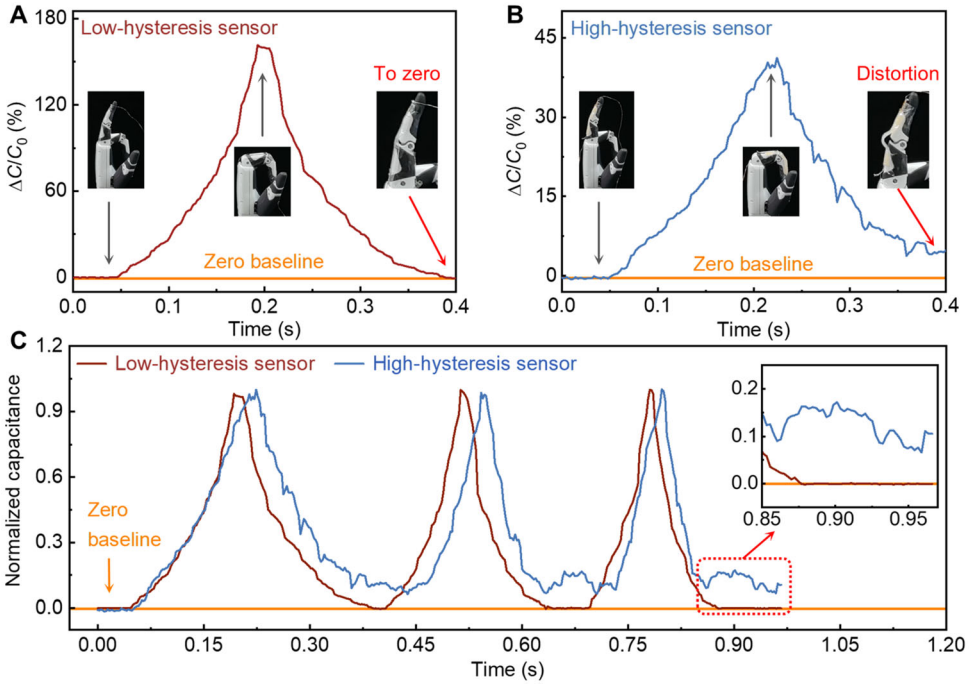

Fig. 6 Accurate strain sensing for robot operation: **A** capacitance change of the low-hysteresis sensor during motion of the robot hand; **B** capacitance change of the high-hysteresis sensor during motion of the robot hand; **C** comparison of the normalized capacitance of the two types of sensors

straightening–bending movements. In each straight state of the PDMS/$IL_{0.3}$-sensor, the change in the capacitance signal could promptly return to zero (Fig. 6A). Visually speaking, the PDMS/$IL_{0.3}$-sensor could always follow the movement of the robot finger and maintain excellent consistency. In contrast, the capacitive signal of the VHB-sensor did not promptly return to zero in the straight state (Fig. 6B). The VHB-sensor exhibits a significant arch when the robotic hand is straightened. Inevitably, the sensor could not remain consistent with the motion state, resulting in a pronounced signal distortion. The hysteresis and signal distortion of the VHB-sensor become increasingly evident as the finger movement speed of the smart robot increases (Fig. 6C). This indicates that hysteresis accumulates continuously and leads to an increasing deviation between the sensor outputs and actual inputs. The application of such a high-hysteresis sensor to the human–machine interaction system would inevitably lead to misjudgment and misoperation of the mechanical device, which contradicts the original intention of building the human–machine interaction system. The PDMS/$IL_{0.3}$-sensor exhibits an exceptionally rapid recovery time, which allows its deformation to be consistent with the motion of the robot. This enables the PDMS/$IL_{0.3}$-sensor to closely follow the movement of the robot, ensuring that the deformation of the sensor accurately reflects the dynamic actions of the robot in real time. This eliminates the hysteresis observed in sensors with longer recovery times, such as the VHB-sensor. Hence, the PDMS/$IL_{0.3}$-sensor has tremendous application prospects in flexible electronics, robotic manipulations, and motion detection.

3.7 The human–machine interaction system based on the low-hysteresis strain sensor and demonstration of its application

Low-hysteresis sensors are promising for applications in wearable devices and human–machine interactions to provide real-time and accurate sensing. As shown in Fig. 7A, the LCR meter measured the capacitance response of the sensor under different movements and then output the capacitance signals to a controller board. This pressed the button on the controller board to record C_{min} and C_{max} when the finger was fully straightened and maximally bent, respectively. When the finger moves within its flexion angle range, the capacitance value also changes between C_{max} and C_{min}, and the opening angle of the robotic hand can be controlled using this capacitance variation.

According to our previous measurements of the performance of the two types of sensors, hysteresis is mainly reflected in the process of release (Fig. 4C–J). This means that the challenge of the sensor with high hysteresis in achieving real-time human–machine interaction is the inaccurate control of the opening action. We conducted a

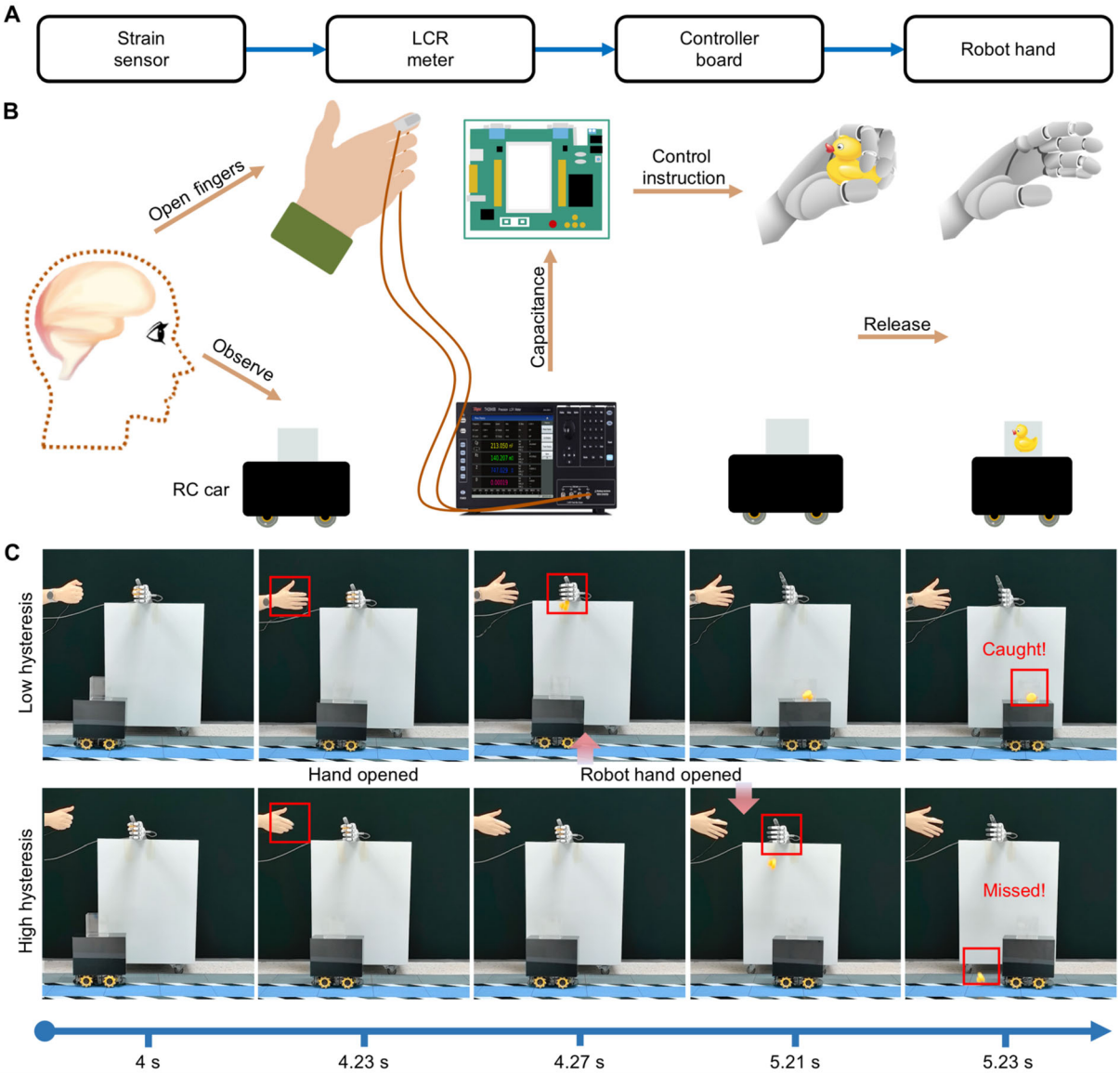

Fig. 7 The human–machine interaction system based on the low-hysteresis strain sensor and its application demonstration: **A** structure of the human–machine interaction system; **B** flow chart of the robot hand controlled by the low-hysteresis strain sensor accurately releasing the duckling; **C** comparison of low-hysteresis and high-hysteresis sensors to control the motion of the robot hand

comparative experiment on the precise delivery of toy ducklings using a PDMS/$IL_{0.3}$-sensor (low-hysteresis sensor) and a VHB-sensor (high-hysteresis sensor). We attached the sensor to a finger of a volunteer when the radio compass (RC) car was observed to be immediately below the robotic hand, and the volunteer opened their hand (at 4.23 s) immediately. The LCR receives the capacitance and transmits information to the controller board through an RS232 serial port. After processing the received information, the controller board controls the opening of the robotic hand (Fig. 7B). When the robotic hand is controlled by the PDMS/$IL_{0.3}$-sensor, the toy duckling successfully falls into a transparent square box fixed to the RC car (Video S3). However, when using the VHB-sensor, the toy duckling did not fall into the box (Video S4). Figure 7C illustrates the distinct responses of both sensors at several representative times. The human hand opens simultaneously at 4.23 s, the PDMS/$IL_{0.3}$-sensor releases the duckling at 4.27 s, and the VHB-sensor releases the duckling at 5.21 s. The response time of the PDMS/$IL_{0.3}$-sensor is only 0.04 s, while that of the VHB-sensor is 0.98 s. These results show that the low-hysteresis PDMS/$IL_{0.3}$ strain sensor is beneficial for accurate and real-time sensing applications.

4 Conclusion

In summary, by fabricating a hyperelastic dielectric layer with high relative permittivity, a hyperelastic encapsulation layer, and a low-hysteresis hydrogel electrode, we successfully developed a flexible strain sensor with ultralow dynamic hysteresis and achieved high-fidelity detection and accurate sensing under large-strain and high-frequency motion. Meanwhile, we used quantitative methods to evaluate the static and dynamic hysteresis levels. Compared with the widely used VHB-sensor, the PDMS/$IL_{0.3}$-sensor demonstrates significant reductions of 21.2- and 4.6-fold in static and dynamic hysteresis, respectively. The PDMS/$IL_{0.3}$-sensor could accurately track the motion of linear motors with dynamic deformation rates up to 500% s^{-1}, yielding an average measurement error of less than 5%. Furthermore, the PDMS/$IL_{0.3}$-sensor exhibits outstanding characteristics, including good stretchability (100%), near-ideal linearity ($R^2 > 0.998$), excellent mechanical stability (> 50,000 cycles), and signal consistency. To demonstrate these excellent features, we developed a human–machine interaction system with real-time, accurate sensing. This work not only overcomes the crucial challenge of developing strain sensors with high-fidelity detection but also paves the way for practical applications in smart sensor systems, wearable electronics, and robot control.

Acknowledgements This work was financially supported by the National Natural Science Foundation of China (Nos. 52250398, 52125205 and U20A20166), the Natural Science Foundation of Beijing Municipality (No. 2222088), Shenzhen Science and Technology Program (No. KQTD20170810105439418), and the Fundamental Research Funds for the Central Universities. The authors also thank Xuzhou B&C Chemical Co. Ltd for providing the photoresist (HTA116, HTA112, B&C Chemicals) used in our work.

Author contributions Yu-Shu Wang contributed to conceptualization, writing—original draft, methodology, investigation, validation, data curation, visualization. Run-Hui Zhou helped in writing—review & editing, methodology, formal analysis, data curation, visualization. Jiao-Ya Huang contributed to conceptualization, methodology, software, formal analysis, visualization. Bo-Ning Sun contributed to conceptualization, formal analysis, visualization. Ze-Min Li was involved in visualization. Zi-Yu Chen was performed investigation. Zhuo-Yu Song done formal analysis. Wen-Chao Gao helped in methodology, formal analysis, supervision, writing—review & editing. Cao-Feng Pan contributed to conceptualization, formal analysis, supervision, project administration, funding acquisition, writing—review & editing.

Data availability The data that support the findings of this study are available from the corresponding author upon reasonable request.

Declarations

Conflict of interests Cao-Feng Pan is an editorial board member for *Rare Metals* and was not involved in the editorial review or the decision to publish this article. All authors declare that they have no conflict of interest.

References

[1] Wan WQ, Liang KM, Zhu PY, Chen XY, Li ZF, Liu SY, Zhang S, Song Y, He P, Wong YH, Zhang SY. Highly stable strain sensor using rGO decorated with multi-component alloy nanoparticles for human motion monitoring. Rare Met. 2024;43(12):6486–99. https://doi.org/10.1007/s12598-024-02890-8.

[2] Mannsfeld SCB, Tee BCK, Stoltenberg RM, Chen CVHH, Barman S, Muir BVO, Sokolov AN, Reese C, Bao Z. Highly sensitive flexible pressure sensors with microstructured rubber dielectric layers. Nat Mater. 2010;9(10):859–64. https://doi.org/10.1038/nmat2834.

[3] Xu MX, Dou C, Song TY, Li X, Zhang Q. A temperature-insensitive silver nanostructures@graphene foam for high accuracy and full range human health monitoring. Rare Met. 2024;43(11):5953–63. https://doi.org/10.1007/s12598-024-02758-x.

[4] Meng XH, Qiao Y, Do C, Bras W, He C, Ke Y, Russell TP, Qiu D. Hysteresis-free nanoparticle-reinforced hydrogels. Adv Mater. 2022;4(7):2108243. https://doi.org/10.1002/adma.202108243.

[5] Xu HC, Liu Y, Mo YP, Chen ZY, Pan XJ, Bao RR, Pan CF. All-fiber anti-jamming capacitive pressure sensors based on liquid metals. Rare Met. 2025. https://doi.org/10.1007/s12598-024-03071-3.

[6] Li YL, Jin XL, Ma YT, Liu JR, Raziq F, Zhu PY, Deng ZF, Zhou HW, Chen WX, Huang WH. Functional decoration on a regenerable bifunctional porous covalent organic framework probe for rapid detection and adsorption of copper ions. Rare Met. 2024;43(2):758–69. https://doi.org/10.1007/s12598-023-02476-w.

[7] Liu K, Li YZ, Wu YX, Ying PJ, He R, Fu CG, Zhang Y, Zhu TJ. Application requirements and design strategies of Bi_2Te_3-based thermoelectric devices for low-quality thermal energy. cMat. 2024;1(1): e11. https://doi.org/10.1002/cmt2.11.

[8] Xu ZH, Sun SS, Li XL, Zhang ZH, Li HY, Ruan ST, Yin SG. Constructing a 3D multichannel structure to enhance performance of Ni-Co-Mn hydroxide electrodes for flexible supercapacitors. Rare Met. 2023;43(1):148–63. https://doi.org/10.1007/s12598-023-02405-x.

[9] Sun K, Zhao MH, Yang PT, Chen M, Hou Q, Duan WX, Fan RH. Negative permittivity of reduced graphene oxide/polyvinylidene fluoride membranous composites adjusted by heat treatment. Rare Met. 2024;43(11):5964–74. https://doi.org/10.1007/s12598-024-02823-5.

[10] Ge G, Lu Y, Qu X, Zhao W, Ren Y, Wang W, Wang Q, Huang W, Dong X. Muscle-inspired self-healing hydrogels for strain and temperature sensor. ACS Nano. 2019;14(1):218–28. https://doi.org/10.1021/acsnano.9b07874.

[11] Dai PF, Zhang Y, Rogozhkin S, Han JH, Li SW, Zhang ZW. Effect of Nb-content on the corrosion resistance of Co-free high entropy alloys in chloride environment. Tungsten. 2024;6(4):778–93. https://doi.org/10.1007/s42864-024-00274-0.

[12] Gao WC, Huang JY, He J, Zhou RH, Li ZM, Chen ZY, Zhang Y, Pan CF. Recent advances in ultrathin materials and their applications in e-skin. InfoMat. 2023;5(8):e12426. https://doi.org/10.1002/inf2.12426.

[13] Bao RR, Tao J, Zhao J, Dong M, Li J, Pan CF. Integrated intelligent tactile system for a humanoid robot. Sci Bull. 2023;68(10):1027–37. https://doi.org/10.1016/j.scib.2023.04.019.

[14] Zhou HW, Zhao C, Zhao ZY, Jiang JC, Jin HL, Wang S, Pan S, Xu MY, Chen YH, Jin HM. Flexible and multifunctional triboelectric nanogenerator based on liquid metal/polyvinyl alcohol hydrogel for energy harvesting and self-powered wearable human-machine interaction. Rare Met. 2023;43(3):1186–96. https://doi.org/10.1007/s12598-023-02518-3.

[15] Zhong S, Lu B, Wang D, Arianpour B, Wang S, Han H, Yin J, Bao H, Liu Y, Wen Z, Zhou Y. Passive isothermal flexible sensor enabled by smart thermal-regulating aerogels. Adv Mater. 2025;37(8):2415386. https://doi.org/10.1002/adma.202415386.
[16] Zhu YL, Cheng WN, Bai YZ, Hou C, Li K, Huang YA. Rise of flexible high-temperature electronics. Rare Met. 2023;42(6):1773–7. https://doi.org/10.1007/s12598-023-02298-w.
[17] He J, Zhou RH, Zhang YF, Gao WC, Chen T, Mai WJ, Pan CF. Strain-insensitive self-powered tactile sensor arrays based on intrinsically stretchable and patternable ultrathin conformal wrinkled graphene-elastomer composite. Adv Funct Mater. 2021;32(10): 2107281. https://doi.org/10.1002/adfm.202107281.
[18] Liu Y, Tao J, Mo YP, Bao RR, Pan CF. Ultrasensitive touch sensor for simultaneous tactile and slip sensing. Adv Mater. 2024;36(21):2313857. https://doi.org/10.1002/adma.202313857.
[19] Tao J, Dong M, Li L, Wang C, Li J, Liu Y, Bao R, Pan C. Real-time pressure mapping smart insole system based on a controllable vertical pore dielectric layer. Microsyst Nanoeng. 2020;6(1):624. https://doi.org/10.1038/s41378-020-0171-1.
[20] Wu WQ, Wang CF, Han ST, Pan CF. Recent advances in imaging devices: image sensors and neuromorphic vision sensors. Rare Met. 2024;43(11):5487–515. https://doi.org/10.1007/s12598-024-02811-9.
[21] Li F, Wang XD, Xia ZG, Pan CF, Liu QL. Photoluminescence tuning in stretchable PDMS film grafted doped core/multishell quantum dots for anticounterfeiting. Adv Funct Mater. 2017;27(17):1700051. https://doi.org/10.1002/adfm.201700051.
[22] He ZP, Han X, Wu WQ, Xu ZS, Pan CF. Recent advances in bioinspired vision systems with curved imaging structures. Rare Met. 2024;43(4):1407–34. https://doi.org/10.1007/s12598-023-02573-w.
[23] Han RH, Liu Y, Mo YP, Xu HC, Yang ZW, Bao RR, Pan CF. High anti-jamming flexible capacitive pressure sensors based on core-shell structured AgNWs@TiO_2. Adv Funct Mater. 2023;33(51):2305531. https://doi.org/10.1002/adfm.202305531.
[24] Wu GC, Li X, Bao RR, Pan CF. Innovations in tactile sensing: microstructural designs for superior flexible sensor performance. Adv Funct Mater. 2024;34(44):2405722. https://doi.org/10.1002/adfm.202405722.
[25] Chen ZY, Zhou RH, Huang JY, Xu HC, Li ZM, Wang YS, Bao RR, He J, Pan CF. Strain-insensitive pre-stretch-stabilized polymer/gold hybrid electrodes for electrochemiluminescent devices. Adv Funct Mater. 2024;34(44):2406434. https://doi.org/10.1002/adfm.202406434.
[26] He J, Wei RL, Ma XL, Wu WQ, Pan XJ, Sun JJ, Tang JQ, Xu ZS, Wang CF, Pan CF. Contactless user-interactive sensing display for human-human and human-machine interactions. Adv Mater. 2024;36(25):2401931. https://doi.org/10.1002/adma.202401931.
[27] Sun XD, Guo X, Zhang JH, Wu J, Shi Y, Sun HY, Pan CF, Pan LJ. A new study on formation mechanism of ordered porous anodized metal oxides. Rare Met. 2024;43(10):5410–8. https://doi.org/10.1007/s12598-024-02802-w.
[28] Li W, Liang T, He X, Oleg V, Pang D, Wu S. Enhanced electric-field induced strain in Eu^{3+} doped $0.67BiFeO_3$-$0.33BaTiO_3$ lead-free piezoelectric ceramics. J Rare Earths. 2024;42(9):1747–54. https://doi.org/10.1016/j.jre.2023.08.001.
[29] He JQ, Wei RL, Ge SP, Guo JC, Tao J, Wang R, Wang CF, Pan CF. Artificial visual-tactile perception array for enhanced memory and neuromorphic computations. InfoMat. 2024;6(3):e12493. https://doi.org/10.1002/inf2.12493.
[30] Huang X, Liu L, Lin YH, Feng R, Shen Y, Chang Y, Zhao H. High-stretchability and low-hysteresis strain sensors using origami-inspired 3D mesostructures. Sci Adv. 2023;9(34):eadh9799. https://doi.org/10.1126/sciadv.adh9799.
[31] He YF, Cheng Y, Yang CH, Guo CF. Creep-free polyelectrolyte elastomer for drift-free iontronic sensing. Nat Mater. 2024;23(8):1107–14. https://doi.org/10.1038/s41563-024-01848-6.
[32] Akhter R, Maktedar SS. MXenes: a comprehensive review of synthesis, properties, and progress in supercapacitor applications. J Materiomics. 2023;9(6):1196–241. https://doi.org/10.1016/j.jmat.2023.08.011.
[33] Zhao E, Wang T, Wang Y, Zeng F, Chen L, Zhu Z, Tang W. Active learning assisted piezoelectric materials synthesis on the basis of composite decision-making. MedMat. 2024;1(2):95–103. https://doi.org/10.1097/mm9.0000000000000006.
[34] Gan YX. Recent development of thermoelectric nanofibers and their composites. J Materiomics. 2023;9(1):99–130. https://doi.org/10.1016/j.jmat.2022.08.009.
[35] Yuan JF, Zhang YZ, Li GZ, Liu SQ, Zhu R. Printable and stretchable conductive elastomers for monitoring dynamic strain with high fidelity. Adv Funct Mater. 2022;32(34):2204878. https://doi.org/10.1002/adfm.202204878.
[36] Xu L, Huang Z, Deng Z, Du Z, Sun TL, Guo ZH, Yue K. A transparent, highly stretchable, solvent-resistant, recyclable multifunctional ionogel with underwater self-healing and adhesion for reliable strain sensors. Adv Mater. 2021;33(51):2105306. https://doi.org/10.1002/adma.202105306.
[37] Wang R, Sun L, Zhu X, Ge W, Li H, Li Z, Zhang H, Huang Y, Li Z, Zhang YF, Zhao J, Xu Q, Lan H. Carbon nanotube-based strain sensors: structures, fabrication, and applications. Adv Mater Technol. 2022;8(1):2200855. https://doi.org/10.1002/admt.202200855.
[38] Liu Y, Tian G, Du Y, Shi P, Li N, Li Y, Qin Z, Jiao T, He X. Highly stretchable, low-hysteresis, and adhesive TA@MXene-composited organohydrogels for durable wearable sensors. Adv Funct Mater. 2024;34(30):2315813. https://doi.org/10.1002/adfm.202315813.
[39] Ko S, Chhetry A, Kim D, Yoon H, Park JY. Hysteresis-free double-network hydrogel-based strain sensor for wearable smart bioelectronics. ACS Appl Mater. 2022;14(27):31363. https://doi.org/10.1021/acsami.2c09895.
[40] Li T, Li X, Yang J, Sun H, Sun J. Healable ionic conductors with extremely low-hysteresis and high mechanical strength enabled by hydrophobic domain-locked reversible interactions. Adv Mater. 2023;35(51):2307990. https://doi.org/10.1002/adma.202307990.
[41] Opris DM, Molberg M, Walder C, Ko YS, Fischer B, Nüesch FA. New silicone composites for dielectric elastomer actuator applications in competition with acrylic foil. Adv Funct Mater. 2011;21(18):3531. https://doi.org/10.1002/adfm.201101039.
[42] Zhou RH, Zhang YF, Xu F, Song ZY, Huang JY, Li ZM, Gao C, He J, Gao WC, Pan CF. Hierarchical synergistic structure for high resolution strain sensor with wide working range. Small. 2023;19(34):2301544. https://doi.org/10.1002/smll.202301544.
[43] Wang R, Qiu T, Zhang Y, Rein M, Stolyarov A, Zhang J, Seidel GD, Johnson BN, Wang A, Jia X. Fiber-based miniature strain sensor with fast response and low hysteresis. Adv Funct Mater. 2024;34(40):2403918. https://doi.org/10.1002/adfm.202403918.
[44] Amjadi M, Kyung KU, Park I, Sitti M. Stretchable, skin-mountable, and wearable strain sensors and their potential applications: a review. Adv Funct Mater. 2016;26(11):1678. https://doi.org/10.1002/adfm.201504755.
[45] Pan CF, Markvicka EJ, Malakooti MH, Yan J, Hu L, Matyjaszewski K, Majidi C. A liquid-metal-elastomer nanocomposite for stretchable dielectric materials. Adv Mater. 2019;31(23):1900663. https://doi.org/10.1002/adma.201900663.
[46] Gallone G, Carpi F, Rossi DR, Levita G, Marchetti A. Dielectric constant enhancement in a silicone elastomer filled with lead magnesium niobate-lead titanate. Mater Sci Eng C. 2007;27(1):110–6. https://doi.org/10.1016/j.msec.2006.03.003.

[47] Yu S, Yu H. Capacitive stretchable strain sensor with low hysteresis based on wavy-shape interdigitated metal electrodes. IEEE Sens J. 2021;21(24):27335–42. https://doi.org/10.1109/JSEN.2021.3124517.
[48] Nur R, Matsuhisa N, Jiang Z, Nayeem MOG, Yokota T, Someya T. A highly sensitive capacitive-type strain sensor using wrinkled ultrathin gold films. Nano Lett. 2018;18(9):5610–7. https://doi.org/10.1021/acs.nanolett.8b02088.
[49] Cuthbert TJ, Hannigan BC, Roberjot P, Shokurov AV, Menon C. HACS: helical auxetic yarn capacitive strain sensors with sensitivity beyond the theoretical limit. Adv Mater. 2023;35(10):2209321. https://doi.org/10.1002/adma.202209321.
[50] Cooper CB, Arutselvan K, Liu Y, Armstrong D, Lin Y, Khan MR, Genzer J, Dickey MD. Stretchable capacitive sensors of torsion, strain, and touch using double helix liquid metal fibers. Adv Funct Mater. 2017;27(20):1605630. https://doi.org/10.1002/adfm.201605630.
[51] Luo Y, Abidian MR, Ahn JH, Akinwande D, Andrews AM, Antonietti M, Bao Z, Berggren M, Berkey CA, Bettinger CJ, Chen J, Chen P, Cheng W, Cheng X, Choi SJ, Chortos A, Dagdeviren C, Dauskardt RH, Di CA, Dickey MD, Duan X, Facchetti A, Fan Z, Fang Y, Feng J, Feng X, Gao H, Gao W, Gong X, Guo CF, Guo X, Hartel MC, He Z, Ho JS, Hu Y, Huang Q, Huang Y, Huo F, Hussain MM, Javey A, Jeong U, Jiang C, Jiang X, Kang J, Karnaushenko D, Khademhosseini A, Kim DH, Kim ID, Kireev D, Kong L, Lee C, Lee NE, Lee PS, Lee TW, Li F, Li J, Liang C, Lim CT, Lin Y, Lipomi DJ, Liu J, Liu K, Liu N, Liu R, Liu Y, Liu Y, Liu Z, Liu Z, Loh XJ, Lu N, Lv Z, Magdassi S, Malliaras GG, Matsuhisa N, Nathan A, Niu S, Pan J, Pang C, Pei Q, Peng H, Qi D, Ren H, Rogers JA, Rowe A, Schmidt OG, Sekitani T, Seo DG, Shen G, Sheng X, Shi Q, Someya T, Song Y, Stavrinidou E, Su M, Sun X, Takei K, Tao XM, Tee BCK, Thean AVY, Trung TQ, Wan C, Wang H, Wang J, Wang M, Wang S, Wang T, Wang ZL, Weiss PS, Wen H, Xu S, Xu T, Yan H, Yan X, Yang H, Yang L, Yang S, Yin L, Yu C, Yu G, Yu J, Yu SH, Yu X, Zamburg E, Zhang H, Zhang X, Zhang X, Zhang X, Zhang Y, Zhang Y, Zhao S, Zhao X, Zheng Y, Zheng YQ, Zheng Z, Zhou T, Zhu B, Zhu M, Zhu R, Zhu Y, Zhu Y, Zou G, Chen X. Technology roadmap for flexible sensors. ACS Nano. 2023;17(6):5211–95. https://doi.org/10.1021/acsnano.2c12606.
[52] Choi DY, Kim MH, Oh YS, Jung SH, Jung JH, Sung HJ, Lee HW, Lee HM. Highly stretchable, hysteresis-free ionic liquid-based strain sensor for precise human motion monitoring. ACS Appl Mater Interfaces. 2017;9(2):1770–80. https://doi.org/10.1021/acsami.6b12415.
[53] Jin H, Nayeem MOG, Lee S, Matsuhisa N, Inoue D, Yokota T, Hashizume D, Someya T. Highly durable nanofiber-reinforced elastic conductors for skin-tight electronic textiles. ACS Nano. 2019;13(7):7905–1780. https://doi.org/10.1021/acsnano.9b02297.
[54] Li S, Liu G, Li R, Li Q, Zhao Y, Huang M, Zhang M, Yin S, Zhou Y, Tang H, Wang L, Fang G, Su Y. Contact-resistance-free stretchable strain sensors with high repeatability and linearity. ACS Nano. 2021;16(1):541–53. https://doi.org/10.1021/acsnano.1c07645.
[55] Wen J, Tang J, Ning H, Hu N, Zhu Y, Gong Y, Xu C, Zhao Q, Jiang X, Hu X, Lei L, Wu D, Huang T. Multifunctional ionic skin with sensing, UV-filtering, eater-retaining, and anti-freezing capabilities. Adv Funct Mater. 2021;31(21):2011176. https://doi.org/10.1002/adfm.202011176.
[56] Xia Q, Wang S, Zhai W, Shao C, Xu L, Yan D, Yang N, Dai K, Liu C, Shen C. Highly linear and low hysteresis porous strain sensor for wearable electronic skins. Compos Commun. 2021;26:100809. https://doi.org/10.1016/j.coco.2021.100809.
[57] Zhu R, Zhu D, Zheng Z, Wang X. Tough double network hydrogels with rapid self-reinforcement and low hysteresis based on highly entangled networks. Nat Commun. 2024;15(1):1344. https://doi.org/10.1038/s41467-024-45485-8.
[58] Wang J, Tang F, Yao C, Li L. Low hysteresis hydrogel induced by spatial confinement. Adv Funct Mater. 2023;33(23):2214935. https://doi.org/10.1002/adfm.202214935.
[59] Huang JY, Zhou RH, Chen ZY, Wang YS, Li ZM, Mo XM, Gao NW, He J, Pan CF. Highly stable and reliable capacitive strain sensor for wearable electronics based on anti-dry hydrogel electrode. Mater Today Phys. 2023;35:101123. https://doi.org/10.1016/j.mtphys.2023.101123.
[60] Shen Z, Zhang Z, Zhang N, Li J, Zhou P, Hu F, Rong Y, Lu B, Gu G. High-stretchability, ultralow-hysteresis conducting polymer hydrogel strain sensors for soft machines. Adv Mater. 2022;34(32):2203650. https://doi.org/10.1002/adma.202203650.
[61] Lee S, Hamonangan WM, Kim JH, Kim SH. Soft and tough microcapsules with double-network hydrogel shells. Adv Funct Mater. 2022;32(34):2203761. https://doi.org/10.1002/adfm.202203761.
[62] Zhong D, Wu C, Jiang Y, Yuan Y, Kim MG, Nishio Y, Shih CC, Wang W, Lai JC, Ji X, Gao TZ, Wang YX, Xu C, Zheng Y, Yu Z, Gong H, Matsuhisa N, Zhao C, Lei Y, Liu D, Zhang S, Ochiai Y, Liu S, Wei S, Tok JBH, Bao Z. High-speed and large-scale intrinsically stretchable integrated circuits. Nature. 2024;627(8003):313–20. https://doi.org/10.1038/s41586-024-07096-7.
[63] Goshkoderia A, Arora N, Slesarenko V, Li J, Chen V, Juhl A, Buskohl P, Rudykh S. Tunable permittivity in dielectric elastomer composites under finite strains: periodicity, randomness, and instabilities. Int J Mech Sci. 2020;186(15):105880. https://doi.org/10.1016/j.ijmecsci.2020.105880.
[64] Freund HJ, Biittner U, Cohen B, Noth J. Time control of hand movements. Prog Brain Res. 1986;64:287–94. https://doi.org/10.1016/S0079-6123(08)63423-8.